

Mechanical properties and energy absorbing capabilities of Z-pinned aluminum foam sandwich

Sajjad Raeisi ^a, Javad Kadkhodapour ^{b, c}, Andres Tovar ^{d, 1}

^a School of Mechanical Engineering, Purdue University, West Lafayette, IN 47907, USA

^b Institute for Materials Testing, Materials Science and Strength of Materials (IMWF), University of Stuttgart, Stuttgart 70569, Germany

^c Department of Mechanical Engineering, Shahid Rajaee Teacher Training University, Tehran 1678815811, Iran

^d Department of Mechanical and Energy Engineering, Indiana University-Purdue University Indianapolis, Indianapolis, IN 46202, USA

Abstract

Aluminum foam sandwich (AFS) structures are suitable for impact protection in lightweight structural components due to their specific energy absorption capability under compression. However, tailoring the deformation patterns of the foam cells is a difficult task due to the randomness of their internal architecture. The objective of this study is to analyze the effect of embedding aluminum pins into an AFS panel (Z-pinning) to better control its deformation pattern and improve its energy absorption capability. This study considers a closed-cell AFS panel and analyzes the effect of multi-pin layout parallel to the direction of the uniaxial compressive loading. The results of the experimental tests on the reference (without Z-pinning) AFS are utilized to develop numerical models for the reference and Z-pinned AFS structures. Physical experiments and numerical simulations are carried out to demonstrate the advantages of Z-pinning with aluminum pins. The results exhibit a significant increase in elastic modulus, plateau stress and energy absorption capability of the Z-pinned samples. Also, the effect of the pin size and Z-pinning layout on the mechanical performance of the Z-pinned AFS is also investigated using numerical simulations.

Keywords: aluminum foam; metal foam Z-pinning; sandwich structure; energy absorption; finite element analysis.

¹ Corresponding Author: Andres Tovar, Department of Mechanical and Energy Engineering, Indiana University-Purdue University Indianapolis, IN, USA, Phone: (317) 278-7090, Email: tovara@iupui.edu

1 Introduction

The design of aircraft and vehicle structures, as well as many other engineering products, is expected to satisfy lightweight and safety requirements. These requirements can be achieved with improvements in cellular materials such as aluminum foam sandwich (AFS) panels. An AFS panel is made of two dense sheets metal (cover sheets) and an internal aluminum foam core. Due to their low density and cellular structure, AFS panels have an outstanding strength-to-weight ratio and unique thermal and acoustic properties [1-7]. Benefits of their use include energy efficiency, low life-cycle cost, acoustic damping, and impact energy absorption [8-10]. When compressed, the aluminum foam core progressively collapses, undergoes large deformations, while maintaining constant compressive stress before the onset of densification [5, 11-13]. This allows AFS panels to dissipate large amounts of impact kinetic energy and makes them suitable for crashworthiness and blast mitigation. In spite of such desirable performance, producing and tailoring the mechanical behavior of an AFS panel is quite tedious and is a topic of active research [14-22].

Several groups have performed related experimental and numerical research on AFS. Mu et al. [15] conducted quasi-static compression tests on aluminum foams and analyzed the deformation mechanisms at the foam cell level. They identified relevant failure modes of closed-cell aluminum foam, which provided insight on the energy absorption mechanisms at the mesoscopic scale. Regarding numerical analysis, Kadkhodapour and Raeisi [4] utilized finite element models of closed-cell aluminum foam and investigated the plateau stress, densification strain, and macroscopic deformation, which explained deformation mechanisms at the macroscopic and mesoscopic scales. Several investigations have been conducted to pursue the reinforcement of composite foams at the microscopic scale through various metallurgy techniques including the addition of Al₂O₃ [16], SiC [17], glass cenospheres [18], and Carbon Nano Tubes (CNTs) [19, 20]. These investigations reported improvements in the mechanical properties of the cell walls; however, the poor bonding between the matrix and the ceramic reinforcements [21] and separation between CNTs on the surface of Al powder [19] are resulted in increasing the brittleness of the composite foam and reduced its energy absorption capacity. Yukun An et al. [23] studied the mechanical properties of a graphene Nano-flakes reinforced aluminum foam (GNF-AF) under quasi-static compressive loading condition. According to the experimental tests, the existence of GNFs can reduce the pore diameter, refine the pore morphology and improve the pore distribution. The stress-strain curve of the aluminum reinforced by GNF was smooth. The plateau stress, energy absorption, and specific energy absorption of GNF-AF were significantly enhanced. Furthermore, the energy absorption efficiency of the modified foam was slightly improved.

Recently, Wang et al. [24] studied the compressive behavior and deformation characteristics of closed-cell aluminum foams prepared by the dynamic gas injection method assisted with high-speed horizontal oscillation. The results obtained from standard compression tests were compared with the mechanical properties of aluminum foams prepared by the static gas injection method. The deformation pattern of the aluminum foam cells was

investigated through the X-tomography of the samples. Their work also showed that, in comparison to the static gas injection method, the dynamic gas injection method produced a significantly reduced foam cell size, which resulted in enhanced mechanical properties. In addition, a number of studies have been carried out to determine the mechanical behavior of regular cellular materials [25-28] and metallic foams [29-37] under dynamic load. Guo et al. [29] investigated the dynamic behavior of an AFS plate under repeated impacts using drop hammer tests with various energy levels. The penetration behavior of the front and back faces was characterized, and the maximum energy absorption was measured after the rupture of the front face. Jing et al. [37] studied the compressive mechanical properties of closed-cell aluminum foams under quasi-static and dynamic loading. A multi-parameter constitutive model was proposed to predict stress as a function of the foam relative density, strain, and strain rate.

A potential alternative technique to tailor the mechanical properties of AFS panels is the use of pins or rods perpendicular to the cover sheets or Z-pinning. Previous studies have demonstrated the effect of Z-pinning in sandwich composites and polymeric foams [38-42]. Mouritz [41] studied the effect of pin size and volume fraction on the through-thickness compression behavior of composites sandwich panels. It was experimentally found that both the effective modulus and the strength of the sandwich structures improved by increasing the volume content and size of the pins. Zhou et al. [42] reinforced foam core sandwiches by embedding composite rods of glass and carbon pin into the holed structures. The compressive impact performance of the reinforced sandwiches was increased because of the embedded composite rods. It has also been reported that the compression strength of the reinforced foams can be optimized through the appropriate selection of rod arrangement and foam density. Despite the potential benefits of Z-pinning in sandwich composites and polymeric foam, research on aluminum foam Z-pinning remains scarce.

This paper investigates the effect of Z-pinning on the mechanical behavior of closed-cell AFS panels. The response of the reference (without Z-pinning) and Z-pinned AFS samples are studied under the quasi-static compressive loading. The numerical models are developed for non-linear finite element analysis of different layout of Z-pinning. Physical Z-pinned AFS samples are also prepared using one pin and four pins. The preparation of the physical samples and the numerical models are described in Sec. 2 and Sec. 3, respectively. The results of the experimental test and the numerical simulations are discussed in Sec. 4.

2 Experimental and numerical procedures

2.1 Preparation of the AFS samples

Aluminum foam sandwich (AFS) samples are prepared from a commercial AFS panel (AFS J-30/2) manufactured by Pohltec® metalfoam GmbH (Cologne, Germany). The material of the cover sheets is aluminum alloy 6082, and the material of the foam core is AlMg₃Si₆ with a relative density (ratio between the aluminum foam density and solid aluminum density) of 15%. The AFS panel used for study is a metallic compound in which the cover sheets are fused to the core layer without adhesive. The AFS nominal height is 30.0 mm, and the thickness of each cover sheet is 2.0

mm. Fig. 1(a) shows the reference AFS samples wire-cut from a larger panel. Fig. 1(b) shows the Z-pinned AFS samples with four pins. The nominal dimension of each AFS sample is 20 mm × 20 mm × 30 mm.

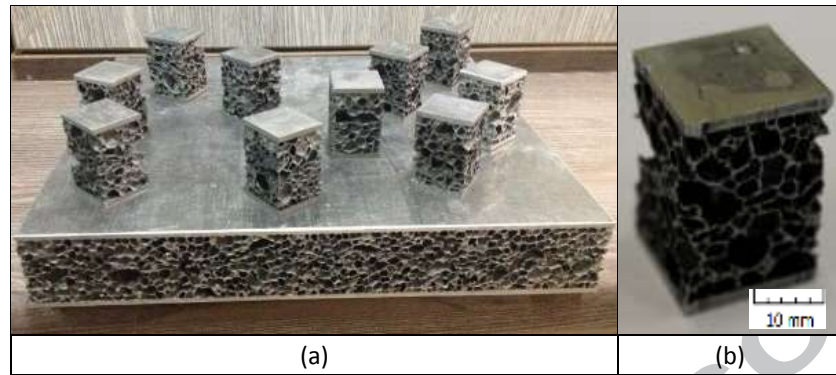


Fig. 1. Aluminum Foam Sandwich samples prepared for the experimental test: (a) Reference AFS samples (without pins) and (b) Z-pinned sample with four pins.

The pins are made of aluminum alloy 1050 with a nominal diameter 3 mm and height 30 mm. For the preparation of the Z-pinned specimens, the AFS samples are perforated, and the pins are perpendicularly press-fitted in the cover sheets to form columns with fixed-fixed ends. The mass of the samples is reported in Table 1.

Table 1. Mass of the AFS samples.

AFS	AFS initial mass (g)	perforated AFS mass (g)	Al pin(s) mass (g)	Z-pinned AFS mass (g)	Mass increase (%)
Reference(s)	7.93 – 8.01	—	—	—	0.0
Z-pinned	7.95	7.52	2.29	9.81	30.45

2.2 Numerical model of the AFS samples

The finite element simulations are carried out using the commercial software Abaqus FEA (SIMULIA, Rhode Island, USA [43]). Fig. 2 (a) shows the reference AFS sample (without pins) and Fig. 2(b) shows the Z-pinned AFS sample with four pins. The non-linear numerical models are comprised of eight-node linear brick finite elements with reduced integration and hourglass control for all the parts. The parts and materials include the cover sheets (Al 6082), the pins (Al 1050), and the foam core (AlMg₃Si₆ with a relative density of 15%). The classical metal plasticity model is used for the cover sheets and the pins, while the crushable foam model is used for foam core [43]. The mechanical properties of the cover sheets, the pins, and the foam (see Appendix A) are reported in Table 2. The plastic hardening data for the aluminum pins (Al 1050) is provided in Table 3.

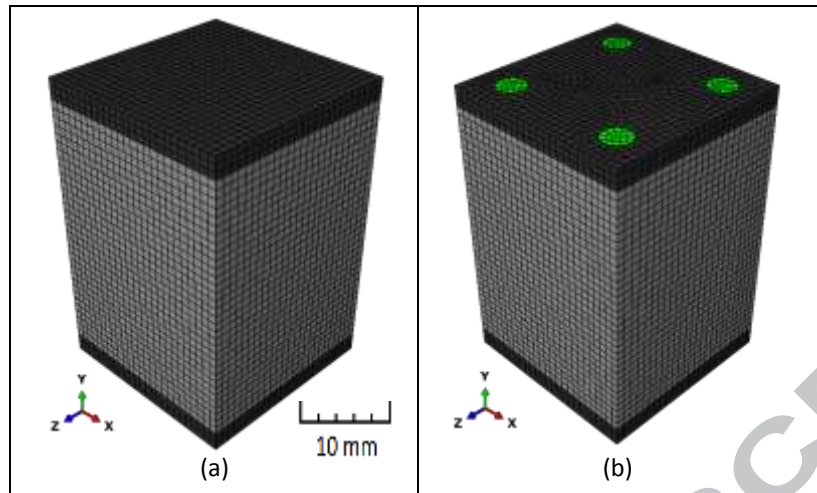


Fig. 2. Finite element models of the AFS samples: (a) Reference AFS sample (without pins) and (b) Z-pinned AFS sample with four pins.

Table 2. Mechanical properties of the cover sheets and the pins.

Mechanical properties	Al alloy 1050 (pins)	Al alloy 6082 (cover sheets)	AlMg3Si6 (foam core)
Elastic modulus	70 GPa	70 GPa	4.89 GPa
Poisson's ratio	0.33	0.33	0.20 (plastic) [44, 45]
Density	2.70 g/cm ³	2.70 g/cm ³	0.41 g/cm ³
Yield strength	87 MPa	250 MPa	—
Ultimate strength	170 MPa	290 MPa	—

Table 3. Plastic stress–strain hardening used for Al alloy 1050 (pins).

Stress (MPa)	Plastic strain (mm/mm)
87	0.0000
96	0.0003
100	0.0020
110	0.0060
130	0.0150
140	0.0250
170	0.0700

The isotropic hardening model is utilized to define the plastic-hardening behavior of the foam. These hardening data are obtained from three experimental uniaxial compression tests (Fig. 3). The testing protocol is described in Sec. 3.1. The characteristic points of the average nominal stress versus nominal strain of the experimental tests are selected and transformed into true (Cauchy) stresses and logarithmic plastic strains [46, 47]. The piecewise linear relationship between the true stress and the logarithmic strain is used to define the hardening property of the foam. The failure criterion for the foam is shear failure [48]. This criterion uses the value of the equivalent plastic strain $\bar{\epsilon}^{Pl}$ at the element integration points. According to this criterion, failure occurs when the equivalent plastic strain exceeds the plastic strain at failure $\bar{\epsilon}_f^{Pl}$. The value of $\bar{\epsilon}_f^{Pl}$ is taken from [49].

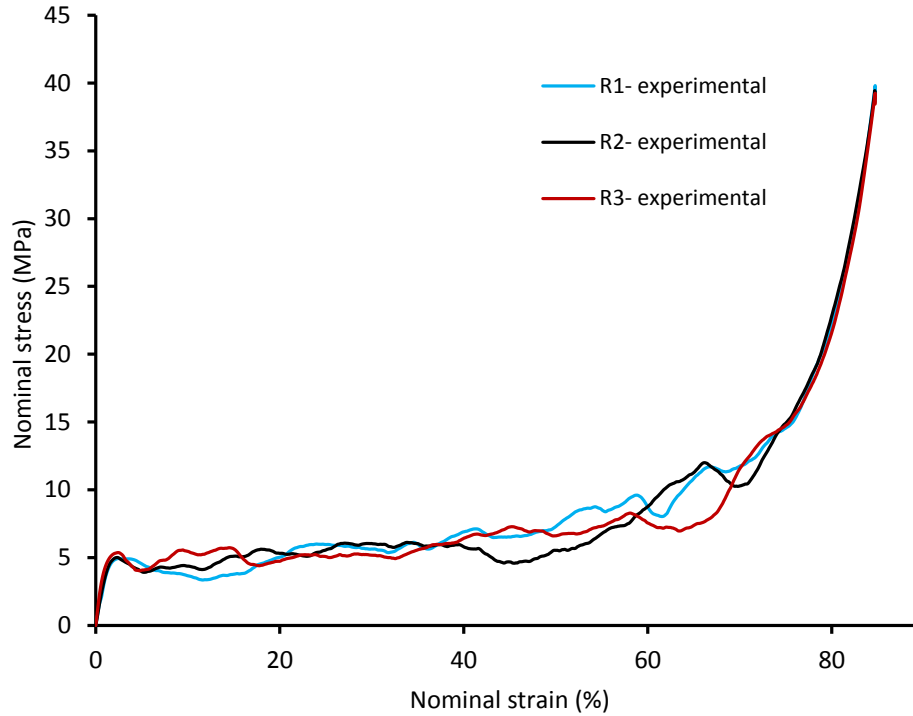


Fig. 3. Experimental results for the stress-strain relation of the reference AFS samples. Data is available at: <https://data.mendeley.com/datasets/3c58tv5k86/1>.

The residual stress due to the press-fit process is not considered in the simulation of the compression test on Z-pinned samples. The stress analysis of the press-fit assembly is provided in Appendix A. The FE simulation indicates that the residual stress arose from press-fit is negligible. A frictionless general contact model is used to prevent interpenetration during the buckling of the pins. Due to the expected large distortion of the foam elements throughout the simulation, Arbitrary Lagrangian-Eulerian (ALE) adaptive meshing technique is employed to mesh the core region of the aluminum foam sandwich. The element size is found to vary in the range of 600 to 1200 microns to analysis the mesh size effect on numerical results. An element elimination scheme is used to remove the damaged elements from the foam core of the Z-pinned AFS. Finally, a boundary condition of displacement is applied to the upper rigid plate in Z-direction, up to 80% of the AFS thickness. The rigid body constraint is used to model the compression fixtures of the universal test machine. The results of the numerical analysis for both the reference and the Z-pinned AFS samples are validated with the experimental data as shown in the following section.

3 Experimental and numerical test of the reference AFS sample

3.1 Experimental test

The samples are subjected to a compressive quasi-static load, uniformly distributed on the cover sheets at a strain rate of $\dot{\epsilon} = 1.3 \times 10^{-3} \text{s}^{-1}$. The deformation and failure of closed-cell AFS under compressive load can be described in two different length scales: macroscopic and microscopic [4, 11]. At the macroscopic scale, the compressive stress-strain curve shows three deformation regimes: linear elastic, stress plateau, and densification (Fig. 4). In the linear elastic regime, which occurs at low strain values, the edges of the foam cells bend, and the faces stretch. This regime is followed by the appearance of deformation bands that triggers the stress plateau regime. During the stress plateau regime, new deformation bands appear and grow progressively collapsing the AFS sample. Finally, once all the AFS sample is fully collapsed, hardening occurs, and the densification regime is initiated. The low relative density of the foam (15%) allows a considerable strain ($\epsilon > 50\%$) before densification appears.

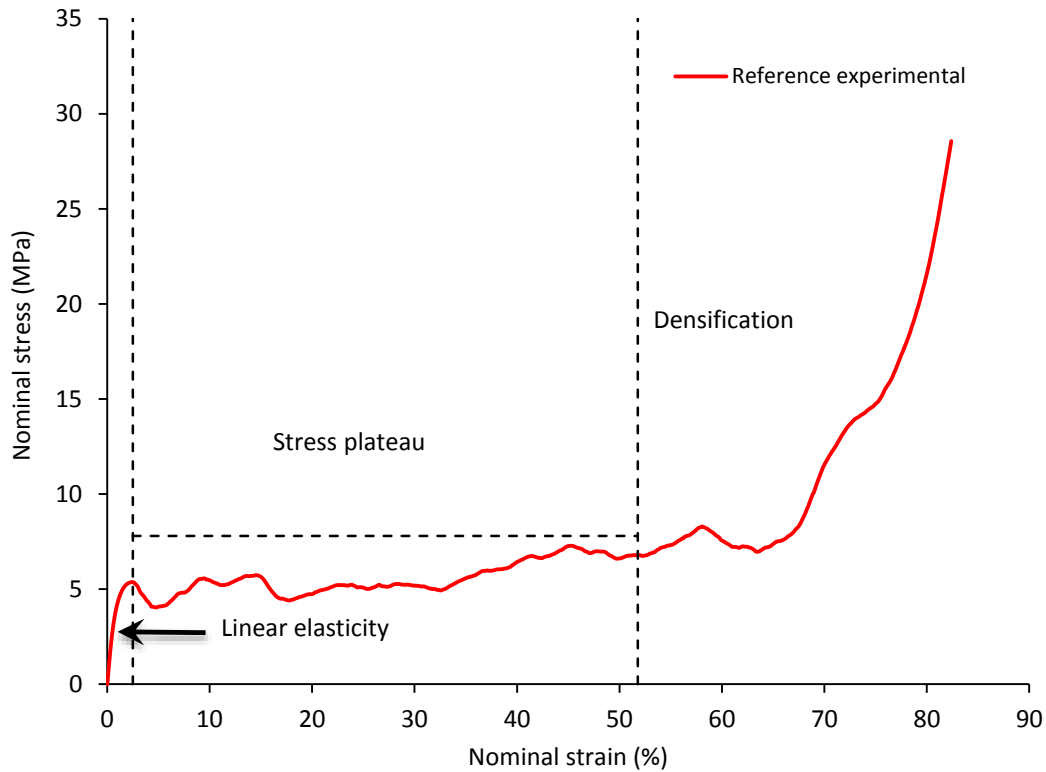


Fig. 4. Experimental stress-strain curve of the AFS without pins (reference sample).

At the microscopic (foam-cell) scale, three deformation modes and four failure modes can be identified [4, 15, 50]. With respect to deformation, Mode I occurs when the foam cell is subjected to uniaxial strain with negligible rotation. Mode II occurs when the foam cell is subjected to uniaxial strain and rotation. Mode III occurs when the foam cell is subjected to uniaxial strain, rotation, and shear. These deformation modes were observed in the compression of the AFS sample (Fig. 5). The deformation mode is substantially determined by the shape of the foam

cell [4, 51]. For ellipsoidal cells, the diameter-width aspect ratio is defined by the ratio of the major and the minor cell diameters. For these cells, the deformation Mode I is predominant if the major diameter is perpendicular to the load and the diameter-width aspect ratio is smaller than 1.2 [52].

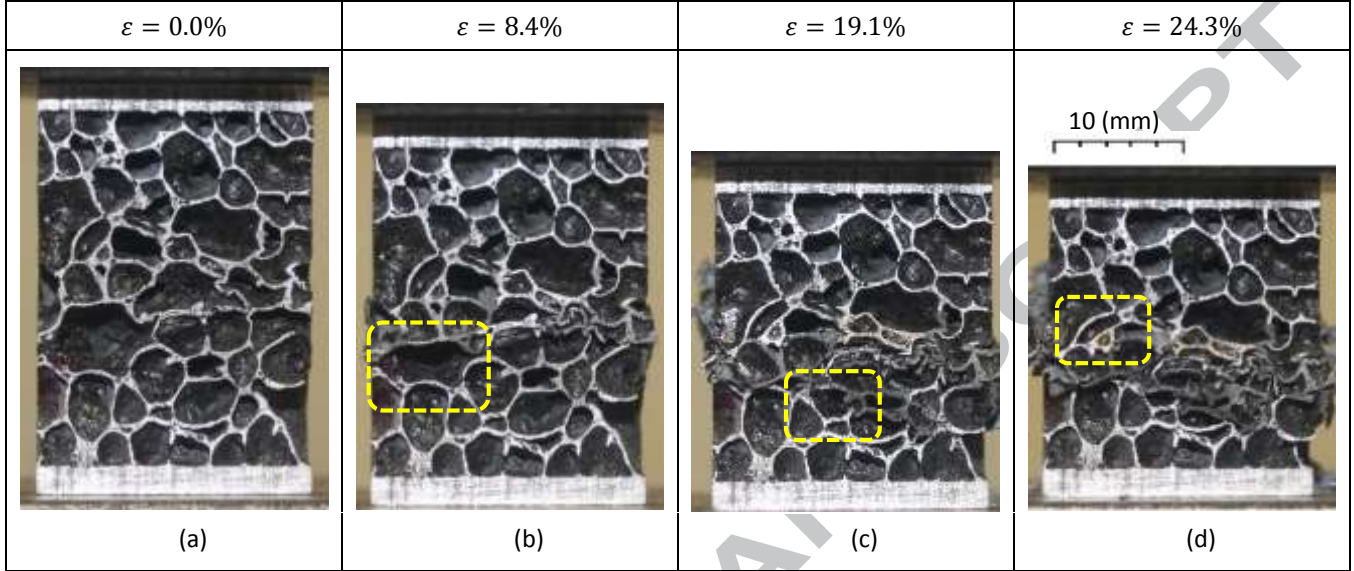


Fig. 5. Representative micrograph of the foam cell deformation: (a) undeformed cells before compression; (b) Mode I cell deformation, (c) Mode II cell deformation, and (d) Mode III cell deformation.

With respect to failure (fracture), four modes can be identified. Mode A is characterized by the bending of the faces and the formation of plastic hinges at the cell walls. Mode B is characterized by the tearing of the cell walls due to tension. Mode C is characterized by the fracture of the cell walls due to shearing. Mode D is characterized by the failure of the cell walls due to the combination of elongation and buckling. For the tested AFS sample, the Mode D failure is observed at relatively high strain values ($\varepsilon > 20\%$). As observed in Fig. 5, lateral elongation is observed at $\varepsilon = 19.1\%$ the buckled faces in the direction perpendicular to the compressive load, which is compatible with Mode A failure. The elongation and buckling tears the cell walls as observed in $\varepsilon = 24.3\%$.

The Scanning Electron Microscopy (SEM) images are utilized to investigate the micro-level failures of the aluminum foam cells (Fig. 6). Failure mode A (bending of the cell walls) and mode D (buckling) is observed in Fig. 6(a). Failure mode B (tearing of the cell walls due to tension) and the corresponding failure and propagation of the cracks is observed in Fig. 6(b). Failure mode C (fracture of the cell walls due to shearing) at the micro level is shown in Fig. 6(c). The cleavage fracture of the brittle aluminum foam cell wall is captured at 60 times magnification in Fig. 6(d).

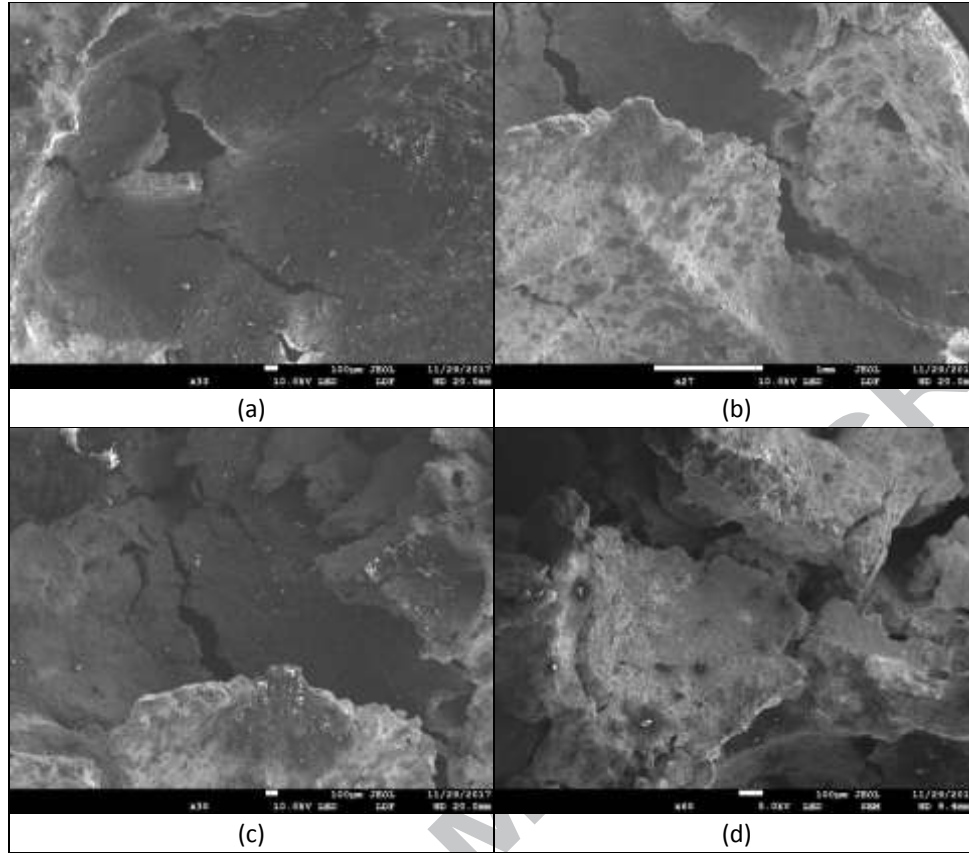


Fig. 6. SEM micrographs of the foam cell walls including the micro-level failures of the cell walls the brittle fracture of AlMg3Si6.

As reported by other studies [15, 53], the deformation and consequent failure of the foam cells occur on the cell walls parallel to the loading direction (Z-direction). The cell walls perpendicular to the loading direction do not undergo significant deformation. Consequently, the perpendicular cell walls do not significantly contribute to the energy absorption process. The addition of pins in the AFS sample is expected to induce new deformation and failure modes and increase the energy absorption capabilities of the foam structure. The effect of Z-pinning with four pins is studied in Sec. 4.

3.2 Numerical simulation

The results of the experimental tests on the reference AFS (without Z-pinning) are utilized to develop the numerical model finite element analysis. The reaction force and the axial displacement of the rigid wall in the compression direction are captured from the FE analysis. The nominal stress is calculated by dividing the force by the initial cross-section, and the nominal strain is obtained by dividing the deformation by the initial height. The numerical and the experimental nominal stress-strain curves are reported in Fig. 7. These curves show a similar behavior characterized by the initial linear elasticity followed by the stress plateau and the densification regime. The

same boundary conditions, material properties, meshing technique, and the geometrical properties of the developed FE model are utilized to simulate the compressive behavior of the Z-pinned AFS samples (Sec. 4).

The distribution of the von-Mises stress through the compression simulation of the reference AFS is shown in Fig. 8. The local stress concentration at $\varepsilon = 9.3\%$ (Fig. 8(b)) corresponds to the local failures and initiation of deformation bands. At $\varepsilon = 18.6\%$ (Fig. 8(c)), the stress distribution is locally uniform. At $\varepsilon = 25.4\%$ (Fig. 8(d)), the stress transitions to a non-uniform distribution, which is a combination of collapsed and non-collapsed regions.

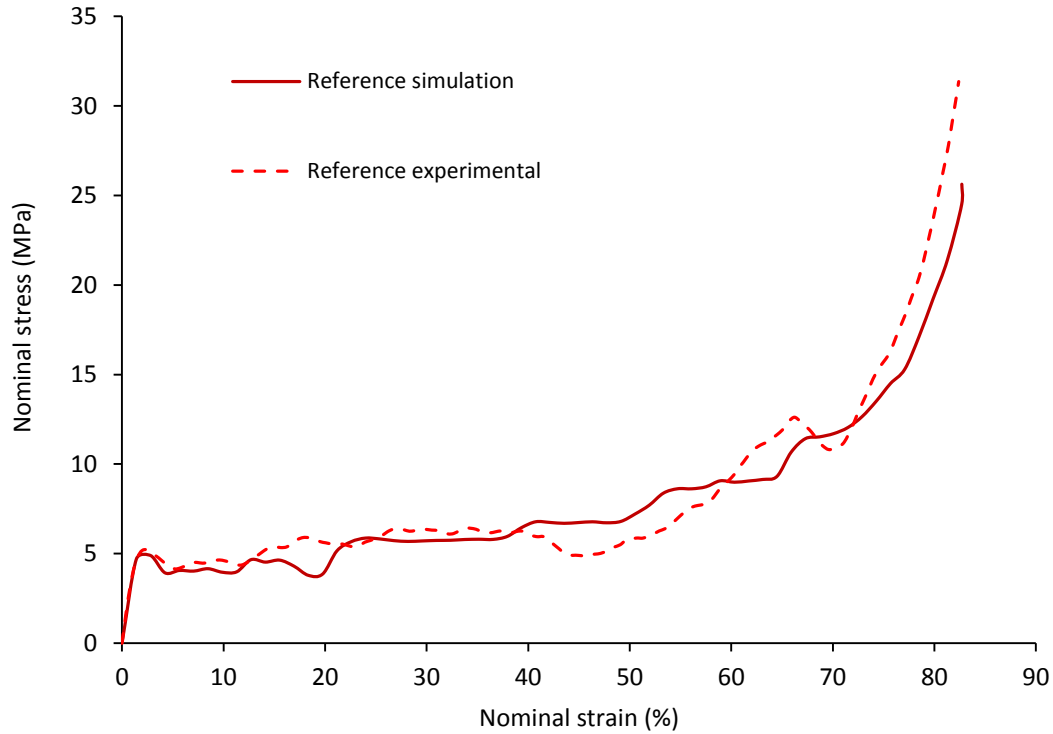


Fig. 7. Experimental and numerical stress-strain curve of the reference AFS sample.

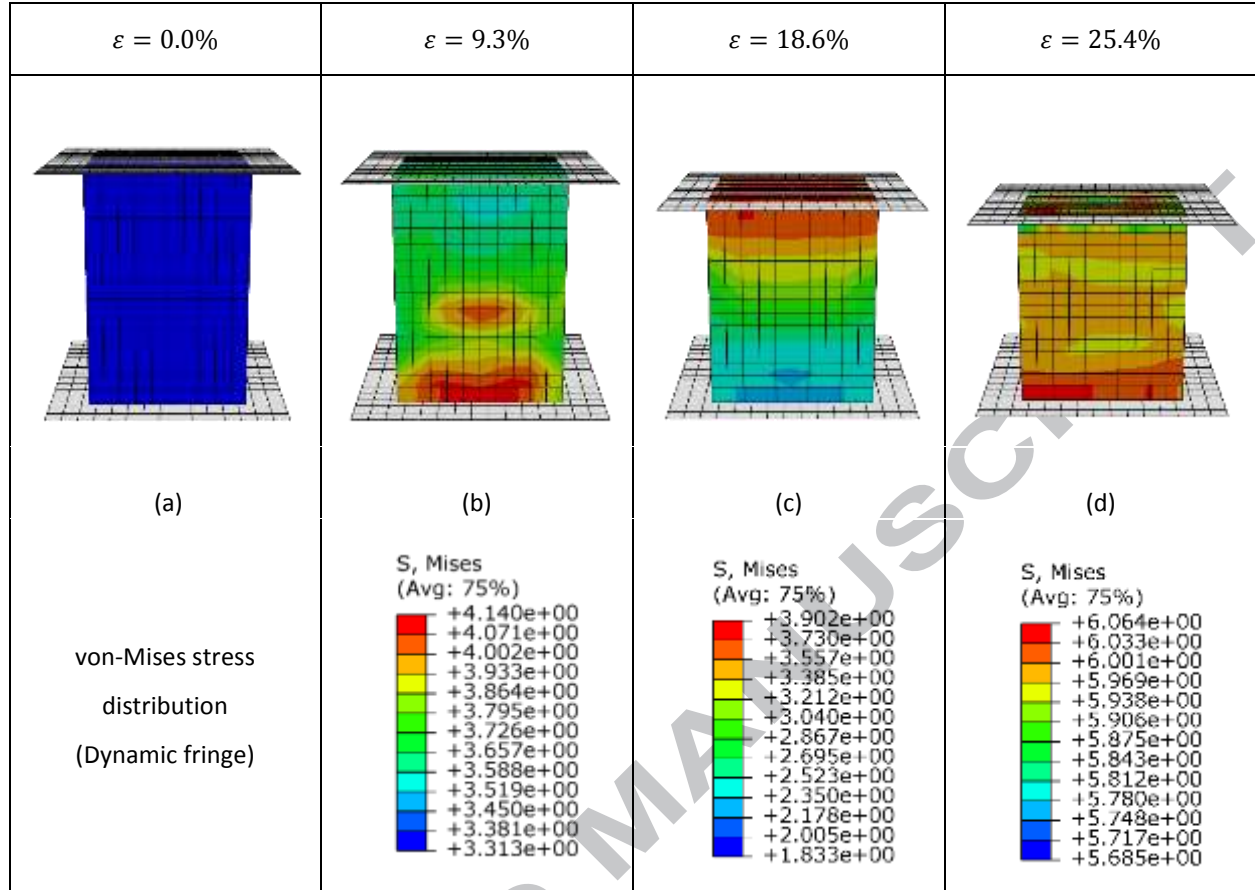


Fig. 8. Numerical simulation of the compression test in the reference AFS sample.

4 Experimental and numerical test of the Z-pinned AFS sample

4.1 Experimental test

The Z-pinned sample is tested under the same mechanical loading and strain rate conditions as the reference sample (Sec. 3.1). The experimental results show that when the loading is applied the pins buckle outwards. When compared to the reference sample, the yield strength of the Z-pinned AFS sample is approximately 2.5 times higher (Fig. 9). The experimental nominal stress of the Z-pinned sample depicts a linear elasticity ($0 \leq \varepsilon < 3\%$) followed by a short stress plateau ($3\% \leq \varepsilon < 8\%$). According to the experimental observation and FEA, the bending of the pins is initiated at this stage. The stability of the pins is enhanced due to the surrounding foam [54]. Since the strain increases, the force on the pins reaches the critical load of equivalent columns. Once the pins buckled, the stress dips following a convex behavior ($8\% \leq \varepsilon < 65\%$). This convex (semi-plateau) region in stress is the result of regular deformations and failures of the undamaged cell pores in the middle of the sample, which carry the load after the pins failure. Finally, a densification regime is observed for $\varepsilon \geq 70\%$.

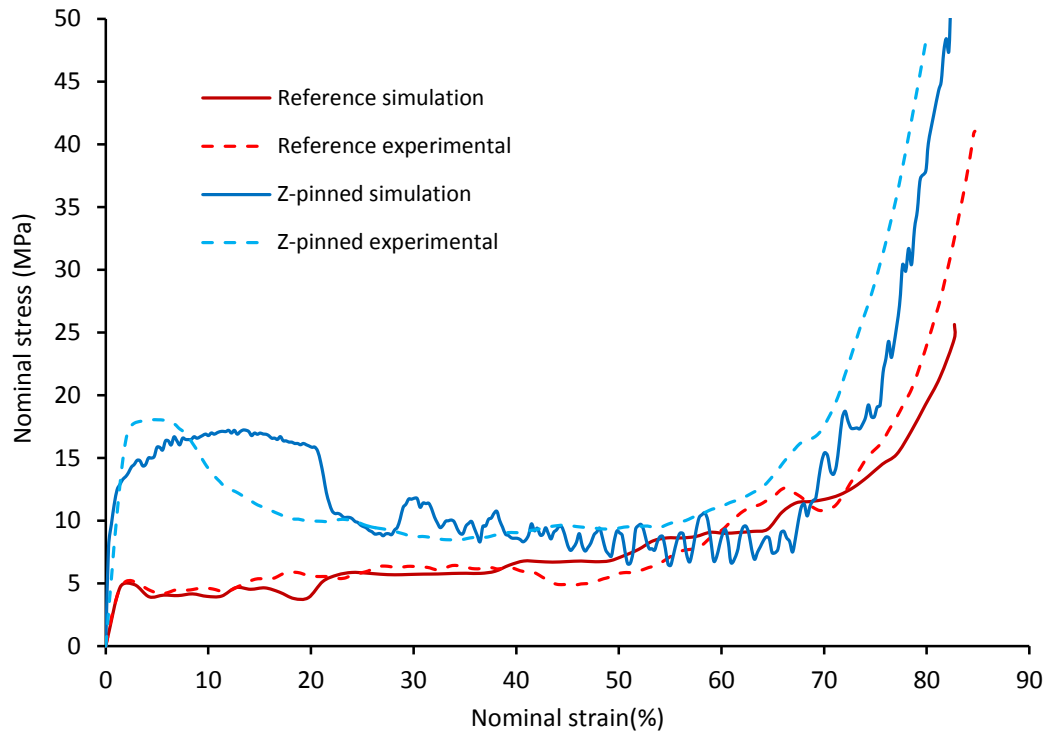


Fig. 9. Experimental and numerical stress-strain curves for the reference and the Z-pinned AFS samples.





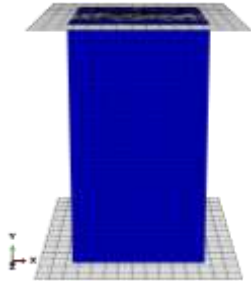
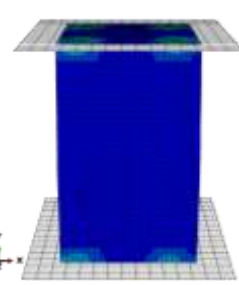
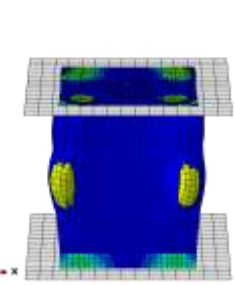
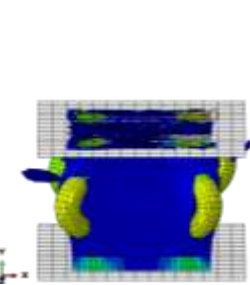
Nominal Strain	$\varepsilon = 0.0\%$	$\varepsilon = 7.2\%$	$\varepsilon = 23.6\%$	$\varepsilon = 36.1\%$
Experimental test				
S, Mises (Avg: 75%)				

Fig. 10. Progress in the buckling of the pins and tearing of the foam material in the Z-pinned samples.

The Z-pinned sample and the corresponding numerical model are shown in Fig. 10. This figure includes the sample prior to the buckling of the pins ($\varepsilon = 0.0\%$). Here, one observes the tearing of foam surrounding the pins once they start buckling ($\varepsilon = 7.2\%$). Further, as the pins continue buckling, they rupture surrounding foam cells ($\varepsilon = 23.6\%$). Increased strain results in reduced buckling strength of the columns and dissection and ejection of parts of the foam ($\varepsilon = 36.1\%$). The additional deformation and crushing of the pins result in the stress values higher than the ones of the reference sample. The pin buckling process and the tearing and rupture of the surrounding foam increase the strain energy absorption capabilities of the Z-pinned sample.

Due to the contact between the foam and the buckled pins, the nominal stress increases during the linear elastic regime. The foam used in this research is brittle; therefore, a small deformation of a pins causes fracture on the adjacent cell walls of the foam. Using foams with ductile walls may further improve energy absorption of Z-pinned AFS structure. The plateau stress regime of the Z-pinned sample is like the plateau stress regime of the reference sample. This regime initiates with the separation of the foam cells adjacent to the buckled pins. At higher strains, the effect of the pins decreases while the remaining foam cells support the load and provide mechanical stability. This can be observed in Fig. 9 where the difference between the nominal stresses of the Z-pinned and the reference samples decreases during the stress plateau regime. The densification regime initiates when the pins are completely buckled, and the remaining foam cells are fully collapsed. During this regime, the nominal stress increases rapidly.

The simulation and experimental results for nominal stress and nominal strain of the Z-pinned samples are in good agreement; however, the behavior of the numerical model shows fluctuations due to the active removal of failed elements. The numerical and the experimental results Z-pinned AFS at $\varepsilon = 43\%$ are shown in Fig. 10. As observed, the pins are fully buckled, and a portion of the foam has been dissection and ejected. The trend of the nominal stress-strain curve shows the supporting role of the pins. The pin buckling and the rupture of the surrounding foam at strain values higher than 50% is observed in Fig. 11. Efficient energy absorption (discussed in Sec. 4.3) continues until the pins erupted out of the foam and the foam cells are collapsed. Due to the current foam brittle nature following by the ruptures, the overall energy absorption capability is declined.

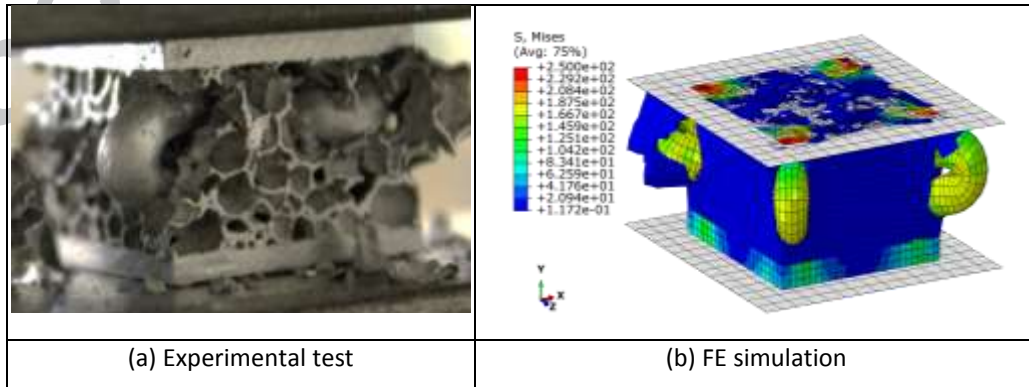


Fig. 11. The completely buckled pin and ruptured surrounding brittle foam in the Z-pinned sample.

4.2 Densification strain and Elastic modulus

The densification strain is an essential characteristic of cellular materials, including the Z-pinned AFS. The densification strain ε_D of the foam inside the reference sample can be obtained from the following equation:

$$\varepsilon_D = \alpha - \beta \bar{\rho}, \quad (1)$$

where $\bar{\rho}$ is the relative density of the foam and α and β are the parameters to include uncertainties factors. For currently available metal foams, α is suggested between 0.8 and 1, and β is between 1.4 and 2 [45, 55]. The importance of the densification strain is that the amount of strain energy is effectively absorbed only at the strain values of $\varepsilon \leq \varepsilon_D$. In a porous material, the densification strain is highly affected by its relative density. The densification stage is initiated with a sharp increase in the stress curve preceded by the plateau region. Even though the relative density of the Z-pinned sample is higher than the reference sample, the densification of the Z-pinned AFS strain is slightly enhanced (Fig. 12).

The elastic modulus of a foam E_f also can be obtained from the following equation:

$$E_f = E_s(\phi^2 \bar{\rho}^2 + (1 - \phi) \bar{\rho}) \quad (2)$$

where E_s is elastic modulus of the solid material and ϕ the distribution constant, is the fraction of solid in the foam that is contained in cell edges. The remaining fraction $(1 - \phi)$ occupies the cell walls. In the case of aluminum, $E_s = 70$ GPa. For the reference AFS sample, the densification strain and the elastic modulus are experimentally determined to be $\varepsilon_D = 67.45\%$. For that sample, the relative density of the foam region is $\bar{\rho} = 15.5\%$, substituting $\alpha = 0.9$ into (1), and substituting $E_f = 4.89$ GPa (2), one obtains $\beta = 1.45$ and $\phi = 0.606$.

For the Z-pinned AFS sample, the densification strain and elastic modulus are experimentally determined to be $\varepsilon_D = 70.34\%$ and $E_{AFS} = 11.2$ GPa. The inverse rule of mixture is employed to drive the effective elastic modulus of the foam region of the Z-pinned AFS (see Appendix A). The elastic modulus of the foam core of the Z-pinned AFS is $E_f^{Z-pinned} = 9.92$ GPa. Adding the mass of the pins, the equivalent relative density of core material of the Z-pinned sample increases to $\bar{\rho} = 22.9\%$. Substituting the values of $\alpha = 0.9$, $\beta = 1.45$, $\phi = 0.606$, and $\bar{\rho} = 22.9\%$ into (1) and (2), the predicted densification strain and elastic modulus of a theoretical unpinned sample with the same relative density as the Z-pinned one are 56.8% and 7.66 GPa, respectively. These values are summarized in Table 4 along with the plateau stress of σ_{pl} —arithmetic mean of the stress at the strain interval between 20% and 30%—, and the energy absorption efficiency (EAE) (Sec. 4.3).

With respect to the reference foam, increasing the relative density results on a decreased densification strain and increased elastic modulus. However, when Z-pinning is utilized, one can observe the following: First, the densification strain remains constant with respect to the reference sample; in other words, the increased mass has

no effect on the stress plateau range. Consequently, the Z-pinned sample can absorb a higher value of strain energy than the theoretical sample with the same density. Second, elastic modulus increases as expected due to Z-pinning and its value is 29% larger than the corresponding prediction for the theoretical unpinned sample.

Table 4. Mechanical properties and specific energy absorption (SEA) for the AFS samples: relative density ($\bar{\rho}$), elastic modulus (E_f), plateau stress (σ_{pl}), densification strain (ε_D), and energy absorption efficiency (EAE).

AFS model	$\bar{\rho}$ (%)	E_f (GPa)	σ_{pl} (MPa)	ε_D (%)	EAE AT ε_D (%)
Reference	15.5	4.89	5.13	67.45	71.72
Z-pinned	22.9	9.92	9.28	70.34	62.32
Theoretical unpinned	22.9	7.66	—	56.8	—

4.3 Energy absorption efficiency

The energy absorption efficiency (EAE) is of great relevance to the characterization of foam materials. EAE is defined as the ratio of the strain energy absorbed by a real material and the strain energy absorbed by an ideal energy absorber [56]. This can be expressed as

$$EAE = \frac{\int_0^{\varepsilon} \sigma d\varepsilon}{\sigma_{\max} \varepsilon}, \quad (3)$$

where σ is the nominal stress, ε is the nominal strain, and σ_{\max} is the maximal nominal stress up to the strain of ε . The first peak (first local maximum) of the EAE-strain curve corresponds to the material yielding strain ε_Y . The last peak (last local maximum) corresponds to the densification strain ε_D [57, 58]. The dashed lines in Fig. 12 indicate the densification strain values for both the reference and the Z-pinned samples. As observed in this figure, the EAE-strain curve of a Z-pinned sample differs from the one of reference AFS. The densification strain of a brittle foam is known to be higher than the one of a ductile foam; however, during the plateau phase, the EAE value of a brittle foam is reported to be 60% or lower [58]. Consequently, the average EAE of a brittle foam is considerably lower than the Z-pinned AFS, which has the maximum of $EAE = 86.73\%$ at $\varepsilon = 8.83\%$ followed by a gradual decline to reach $EAE = 62.32\%$ at its densification strain $\varepsilon_D = 70.34\%$ (Fig. 12). The EAE-strain curve of the Z-pinned sample is smoother, similar to the one of a ductile foam; however, the smoothness of the curve in the ductile foam is caused by the sequential collapse of the foam cell, while the smoothness of the EAE curve of the Z-pinned sample is due to the continuous buckling of the pins. Remarkably, the densification strain of Z-pinned sample and brittle foams are found to be significantly higher than the one of ductile foams [58].

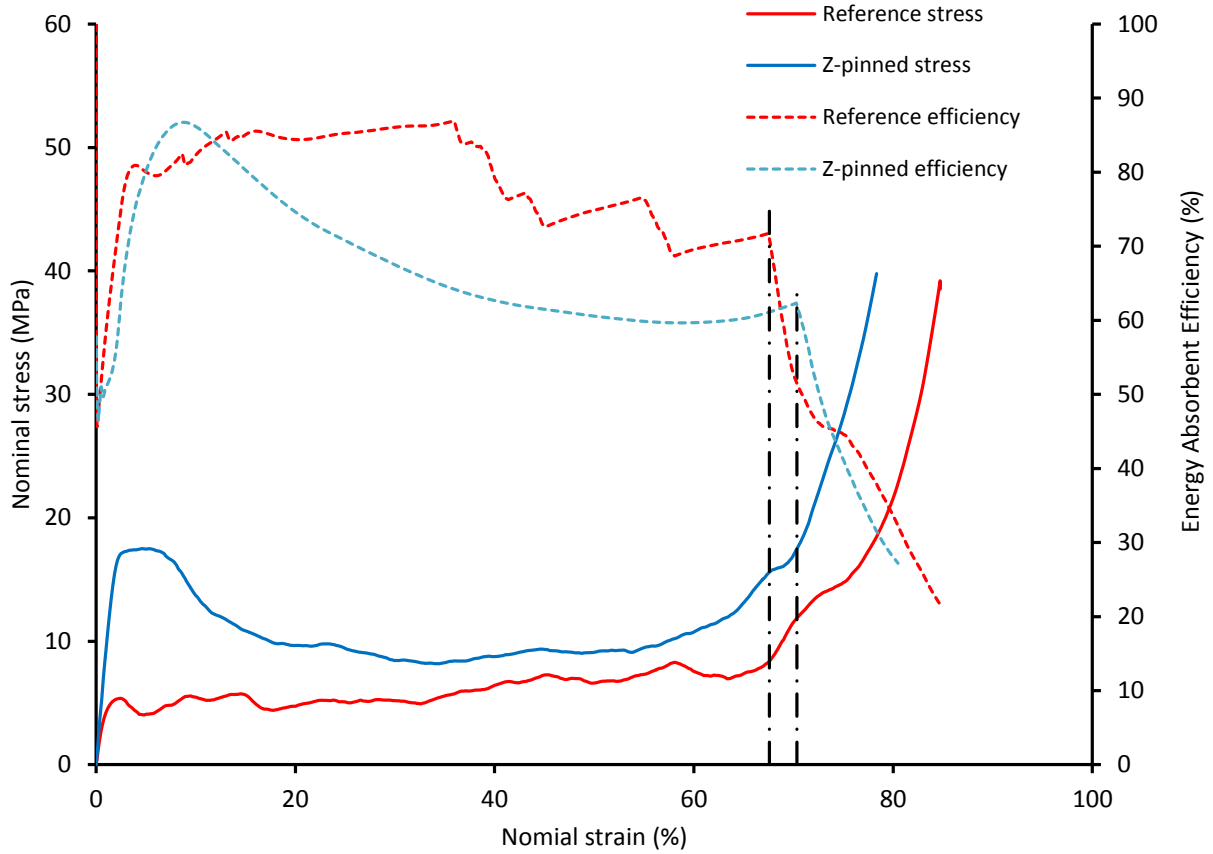


Fig. 12. Relationship between the energy absorption efficiency and the compressive stress for the reference AFS and the Z-pinned AFS sample.

4.4 Total energy absorption

The total energy dissipation E of an AFS sample under compression can be expressed as:

$$E = \int_0^{\varepsilon} \sigma d\varepsilon = E_b + E_m + E_{frac} + E_g + E_{fric} + E_{buck} + E_{rupt}, \quad (4)$$

where E_b , E_m , E_{frac} , E_g , and E_{fric} represent the energy absorbed due to bending, deformation in membranes, fracture of walls, pressure of a gas trapped inside the pores, and friction due to contact between walls, respectively; E_{buck} represents the energy absorbed due to the bucking of the pins; and E_{rupt} represents the energy absorbed due to the rupture of the foam cells surrounding the pins. The mechanisms of energy dissipation for E_b , E_m , and E_{frac} terms are discussed in Sec. 3.1. If the cell walls do not rupture under the compression, the gas trapped within the cells is compressed and the elastic modulus of the closed cell foams increase. The friction mechanism of energy dissipation (E_{fric}) usually occurs at high strain values, when the deformed cells come into contact with one another. The first five energy dissipation mechanisms (E_b , E_m , E_{frac} , E_g , and E_{fric}) are considered in both the reference and the Z-pinned samples. The last two terms (E_{buck} and E_{rupt}) are considered only in the Z-pinned sample.

A measure for the Energy Absorption Improvement (EAI) of the Z-pinned sample is defined in this work as

$$\begin{aligned} \text{EAI} &= \frac{E_{Z\text{-pinned}} - E_{\text{reference}}}{E_{\text{reference}}} = \frac{E_{\text{buck}} + E_{\text{rupt}}}{E_b + E_m + E_{\text{frac}} + E_g + E_{\text{fric}}} \\ &= \frac{\int_0^\varepsilon \sigma_{Z\text{-pinned}} d\varepsilon - \int_0^\varepsilon \sigma_{\text{reference}} d\varepsilon}{\int_0^\varepsilon \sigma_{\text{reference}} d\varepsilon}, \end{aligned} \quad (5)$$

where $E_{Z\text{-pinned}}$ and $E_{\text{reference}}$ represents the total strain energy absorbed by the Z-pinned AFS and the reference AFS samples, respectively.

Experimental compression tests are carried out on three reference samples identified as R1, R2, and R3 to evaluate EAI (Fig. 13). Improvement in the amount of absorbed energy in the Z-pinned AFS is compared to three reference samples

The dissipated strain energy by the Z-pinned AFS is approximately 250% higher than the reference samples while the nominal strain is less than 10%. As discussed in the previous sections, for the strain values in the range $10\% \leq \varepsilon < 40\%$, the nominal stress and EAE decline because of emerging the buckling in the pins and disintegration of the foam material. For the strain values higher than 40%, the undamaged foam cell located near the center of the Z-pinned AFS absorbs strain energy and EAI curves decline gradually with gentler slopes in Fig. 13. Although the main trend of the EAI curves is descending, the minimum value of the EAI curves (at strains about 65%) indicate the energy absorption improvement of 60%. It means that the amount of absorbed energy by Z-pinned AFS is at least 1.6 times higher than that of reference AFS samples.

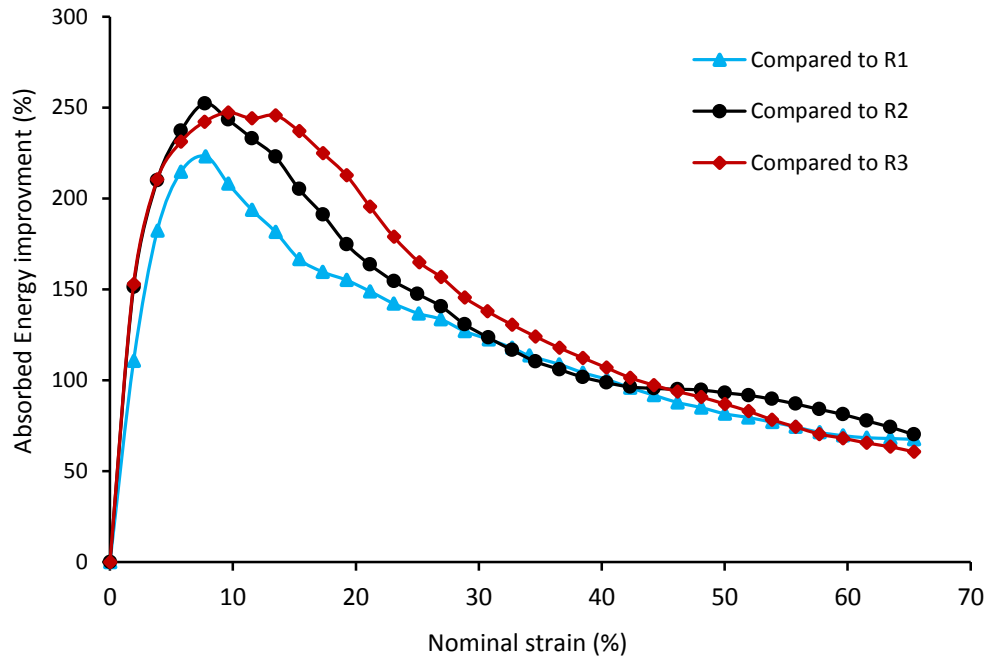


Fig. 13. Energy absorption Improvement of the Z-pinned samples compared to the reference samples.

4.5 The effect of the Z-pinning layout

The developed FE model for the reference AFS sample is further used to study the effect of the number, size, and material properties of the pins on the mechanical performance of the Z-pinned AFS structures. The FE model of the four Z-pinning layouts with one, two, three, and four pins are prepared to investigate the effect of the number of pins on the mechanical response of the Z-pinned AFS. All these AFS samples are Z-pinned using aluminum pins with a radius of 1.5 mm. The FE model and buckling modes of the pins for are shown in Fig. 14. The mechanical responses of these four models are obtained using the same boundary and loading conditions as the reference one.

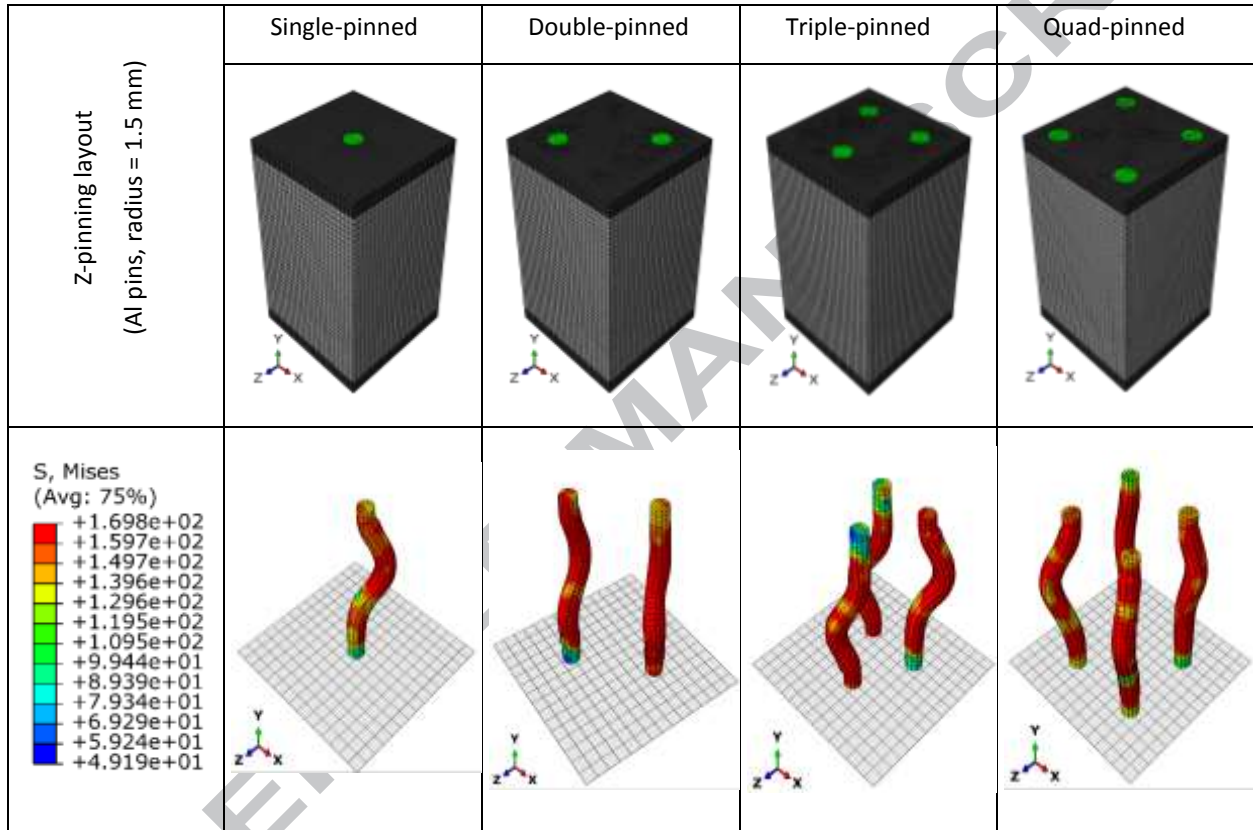


Fig. 14. The FE models of AFS structures with different Z-pinning layouts.

The stress-strain relationships of these Z-pinned AFS samples are shown in Fig. 15. Due to the buckling of the pins, the nominal stress values significantly drop for all the Z-pinned samples. The failure of the pins occurs at a strain between 20% and 22%. The stress-strain curves indicate that stress drop due to the pin failure reduced with an increased number of the pins. For instance, the nominal stress of the single-pinned sample drops by 78% from 7.4 MPa to 1.6 MPa while the stress of the quad-pinned sample decreases by 45% from 16.0 MPa to 8.8 MPa.

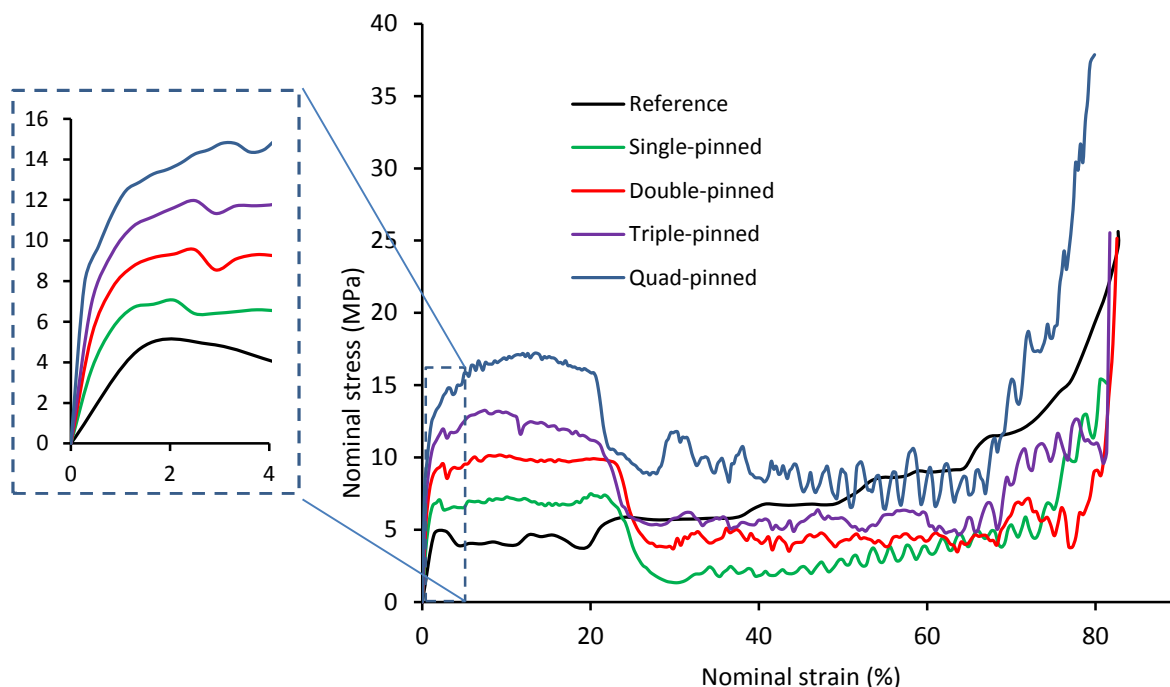


Fig. 15. Stress-strain relationship for the AFS samples with different layouts of the pins.

These numerical results indicate the importance of the match between the AFS cross-sectional shape and the pattern of the Z-pinning (Fig. 16). The plateau stress of the single-pinned sample is 4.32 MPa, compared to 5.45 MPa of the reference AFS. The experimental results also show that the single-pinned models are notoriously unstable and Z-pinning of square -shape AFS with one pin is comparably inefficient (see Appendix C). The stability of the Z-pinned AFS structure significantly enhanced by increasing the number of pins. The plateau stress of the triple-pinned sample is slightly higher than the double-pinned sample; 7.0 compared to 6.6 MPa. However, the plateau stress of the Quad-pinned sample is 10.7 MPa, which is 53% higher than the triple-pinned sample. The quad-pinned layout has the highest ratio between the plateau stress to mass for the square-shape AFS. This remarkable improvement is due to the match between the symmetrical shape of the AFS sample and Z-pinning layout.

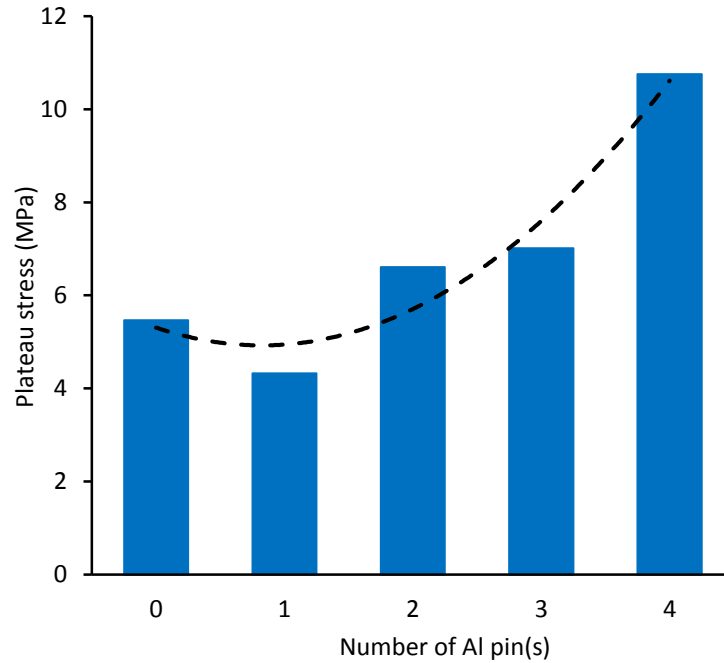


Fig. 16. The effect of the pin number on plateau stress of the Z-pinned AFS samples.

4.6 The effect of the pin size

The FE analysis is also employed to study the effect of the pin size on the mechanical behavior of the Z-pinned AFS. Three different values of radius (1.0 mm, 1.5 mm, and 2.0 mm) are used to model the Z-pinned AFS samples with aluminum pins. Furthermore, the aluminum pins with a radius of 1.5 mm are replaced with Steel ones with the same dimension to illustrate the effect of the pin mechanical properties. The stress-strain relationships for the quad-pinned samples of various pin sizes are shown in Fig. 17. Increasing the size or stiffness of the of the embedded pins directly increases the elastic modulus of the Z-pinned structure. Also, the strain corresponding to the failure of the pins alters with both the size and material properties parameters of the pins. However, the mechanical response of a Z-pinned AFS structure at higher strain values is not consistently changing based on these parameters. For instance, the Al pins with a radius of 1.0 mm, and 2.0 mm fail at the strain values of 15.0% and 5.8%, respectively. The failure of the pins with the radius of 1.5 mm occurs at the strain of 20% for Al pins and 30% for Steel pins. Furthermore, the densification strain of the Z-pinned sample is highly dependent on the pin dimension, and it is inversely proportional to the pin radius.

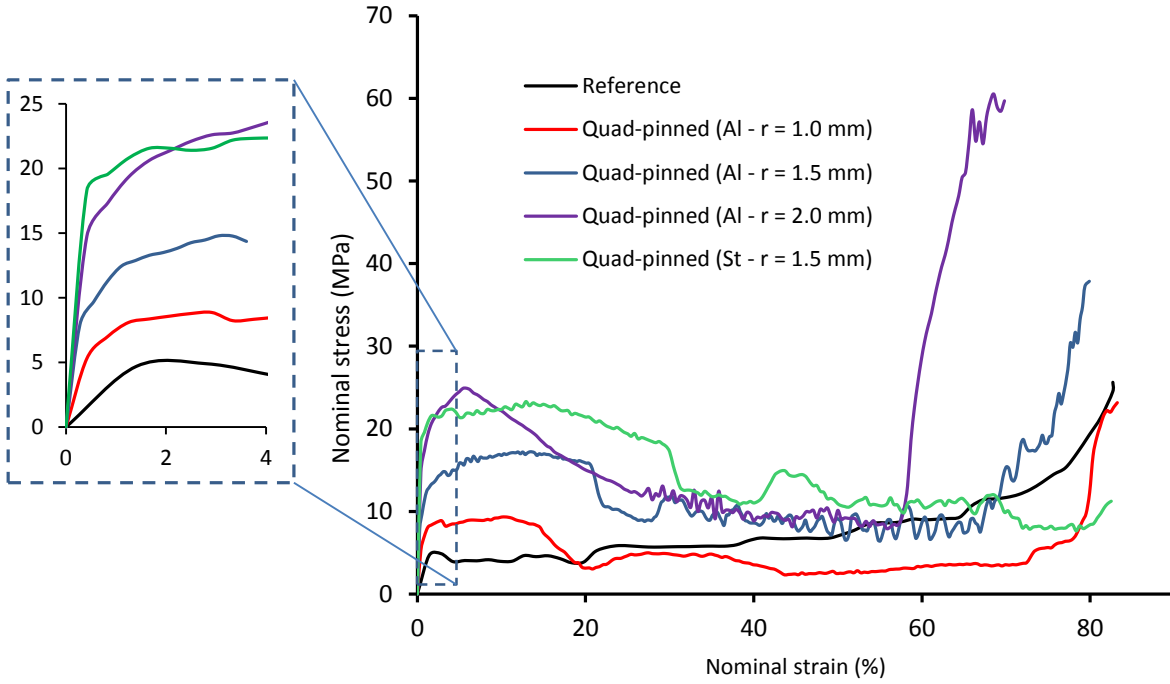


Fig. 17. Stress-strain relation for the AFS samples with different size of the pins.

Fig. 18 shows the effect of the pin size on the plateau stress of the quad-pinned AFS samples. The plateau stress of the sample with pin radius of 1.0 mm is 20% less than the reference sample, although its elastic modulus is significantly improved. The buckling of the pins results in tearing of the foam and separation of some undeformed foam materials. For the Z-pinned structures with small pin radius, the destructive effect of the foam removal dominates the strength improvement due to the buckling of pins. Instead, the proper pin dimension substantially increases the plateau stress of the Z-pinned AFS. For instance, the plateau stress of the Z-pinned AFS with pin radius of 1.5 mm is 10.75 MPa, which is 97% enhanced in comparison to the reference AFS with plateau stress of 5.46 MPa. In addition, the material properties of the pin directly affect the deformation pattern of the pins and plateau stress of the Z-pinned AFS. The plateau stress of the Z-pinned sample with Steel pins (elastic modulus of 207 GPa) is 257% higher than the reference sample and 82% higher than the similar structure Al pins of the radius of 1.5 mm.

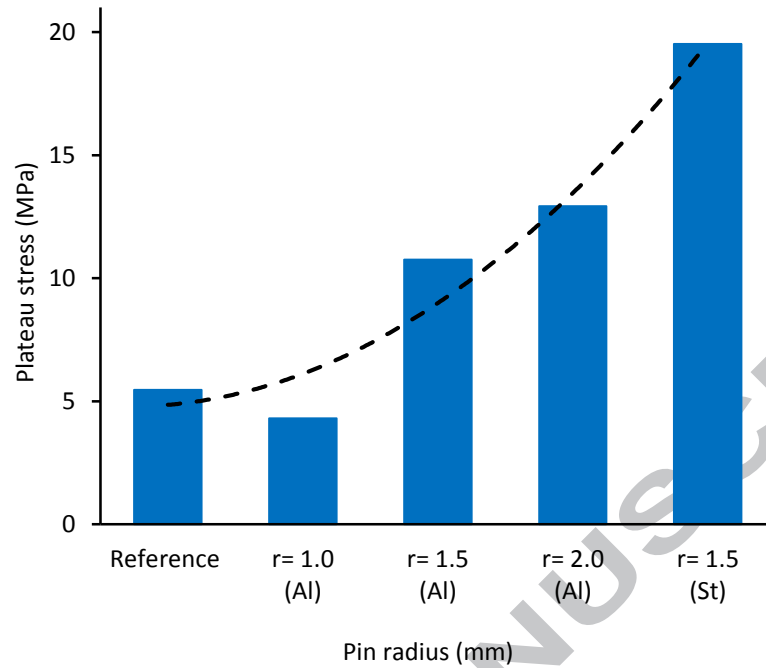


Fig. 18. The effect of the pin size on plateau stress of the Z-pinned AFS samples.

5 Conclusion

In this research, three Aluminum Foam Sandwich (AFS) samples were tested under the quasi-static condition to characterize the mechanical properties of the foam core. The SEM imaging and physical test were utilized to study the different micro-failure modes and the deformation of the closed-cell aluminum foams, respectively. Moreover, a Finite Element (FE) model of the reference AFS structure was developed based on the experimental results. Some other reference AFS samples were modified by Z-pinning to enhance their energy absorption capability under compressive loading. The mechanical properties of the Z-pinned AFS samples were compared with those of the reference structures using the experimental compression tests and the non-linear FE simulations. The energy absorption behavior and the load-bearing capacity of the Z-pinned AFS were characterized. The elastic modulus of the Z-pinned foam increased from 4.89 GPa to 9.92 GPa, and the plateau stress of the Z-pined sample improved to 9.28 MPa, compared to 5.13 MPa of the reference AFS. Although the Z-pinned AFS sample had a larger relative density, the densification strain of the Z-pinned AFS structure remained the same as the reference one. Furthermore, the Z-pinned sample absorbed a substantial amount of strain energy at the low strain values, while the energy absorption efficiency was also comparably higher than the reference sample. The pins buckling, and cell walls tearing were determined as the additional failures in the Z-pinned AFS. Eventually, the effect of pin size and Z-pinning layouts were investigated using the numerical simulations. The potential improvement on the mechanical behavior of the novel Z-pinned AFS can be obtained by optimizing the stiffness ratio values between the pins and the foam inside the AFS, dimensions, and layout of the Z-pinning.

Acknowledgements

The authors would like to acknowledge Daniel Minner from Integrated Nano-systems Development Institute at Indiana University-Purdue University Indianapolis for his assistance with training and capturing the Scanning Electron Microscopy (SEM) images. The authors also would like to show their gratitude to Dr. Korbinian Heim from Pohltec® metalfoam GmbH for providing the material properties of the sandwich panels.

6 Appendices

6.1 Appendix A: Elastic modulus of the foam

The elastic moduli E_{AFS} of three reference AFS samples are obtained from experimental tests under quasi-static condition with values 5.87 GPa, 5.12 GPa, and 5.76 GPa. The corresponding elastic modulus of the foam phase is derived from the rule of mixtures. The schematic model of the AFS structure is shown in Fig. A. 1.

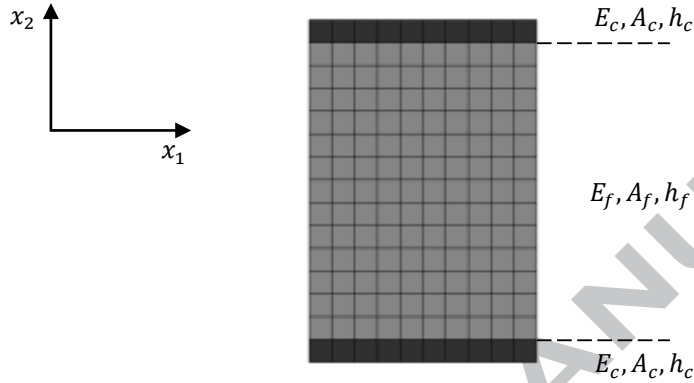


Fig. A. 1: Schematic model of the AFS structure.

The cover sheets have thickness h_c , area A_c , and elastic modulus E_c . The foam phase has thickness of h_f , area A_f , and elastic modulus E_f . Considering the loading in direction x_2 , the equilibrium equation is

$$\sigma_{AFS} A_{AFS} = \sigma_c A_c = \sigma_f A_f, \quad (6)$$

where σ is the normal stress. Since the area is the same, then $\sigma_{AFS} = \sigma_c = \sigma_f$. Similarly,

$$\epsilon_{AFS} h_{AFS} = 2\epsilon_c h_c + \epsilon_f h_f, \quad (7)$$

where ϵ is the corresponding normal strain. Applying Hooke's law and defining the volume fraction of cover sheet as $f_c = 2h_c/h_{AFS}$ and the volume fraction of the foam as $f_f = h_f/h_{AFS}$, yields

$$E_{AFS} = \frac{E_c E_f}{f_f E_c + f_c E_f}. \quad (8)$$

Finally, the mean elastic modulus of the reference AFS samples $E_{AFS} = 5.58$ GPa and the elastic modulus of the aluminum cover sheets $E_c = 70$ GPa are substituted into (8) to find the elastic modulus of the foam $E_f = 4.89$ GPa. This value is in good agreement with the value of 5.0 GPa reported by the manufacturer.

6.2 Appendix B: Press fit model

The stress analysis of the press fit is carried out to investigate the effect of the press fit assembly on the residual stress arose in the Z-pinned AFS. Due to the symmetric geometry of the model, only one-quarter of the Z-pinned AFS is considered to study the residual stresses. The estimated diametric interference of 0.010 mm is considered to analyze the residual stress of the press fit process. The pin model has a nominal diameter of 3.0 mm, and the diameter of the cover sheet is reduced to consider the diametric interference. Fig. B. 1 shows von-Mises stress distribution of the cover sheet, the pin, and the foam region after the assembly of Z-pinned AFS. The maximum stress of 101 MPa occurs at the top and bottom ends of the pin. Due to the stiffness of the cover sheets, the stress at the pin ends goes beyond the yield strength of Al 5010. However, the stress distribution on the pin section embedded within the foam core indicates remarkably lower values with the maximum of 10 MPa. This lower residual stress is because of the comparable small stiffness of the surrounding foam. The regions around the holes on the cover sheets reach the yield strength of Al 6082 (250 MPa) due to the residual stress concentration generated by press fit process. However, at the regions far from the holes, two times of the pin diameter and beyond, the residual stress is almost zero in the cover sheets. The effect of the residual stress is neglected in the compression test simulation because of two reasons. First, only the top and bottom regions of the pin are profoundly affected by the press fit assembly. The effect of residual stress in these regions is negligible in buckling of the pins. Second, the residual stress generated in the AFS sample is insignificant in distances beyond five mm in cover sheets or beyond three mm in the foam.

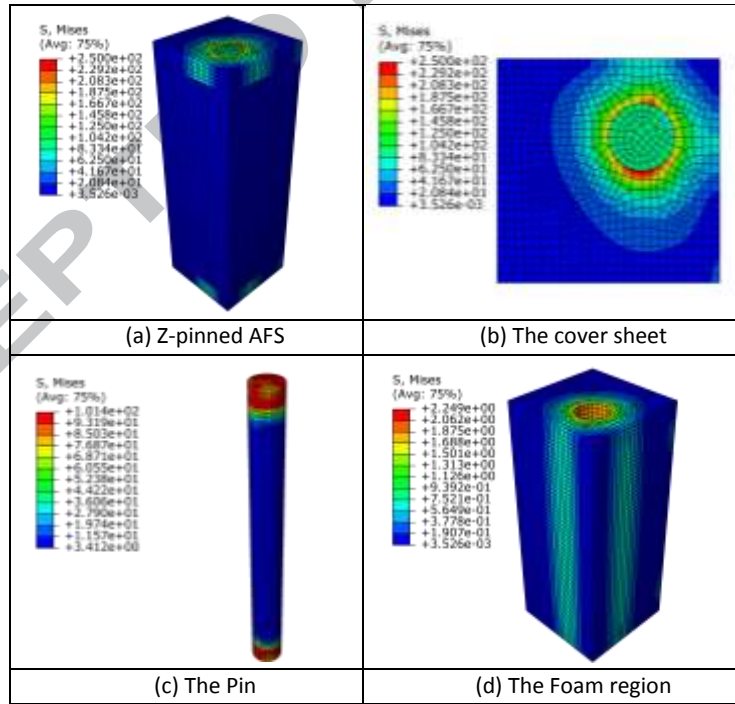


Fig. B. 1: The von Mises residual stress distribution in the components of the Z-pinned AFS.

6.3 Appendix C: Experimental results of a single-pinned AFS

The single-pinned AFS samples are notoriously unstable under the compressive loading. The upper and the lower cover sheets of the sandwich slide on each other in the direction of the pin buckling. As it is illustrated in Fig. C. 1 the cover sheets slipped on each other, out of the main loading axis.



Fig. C. 1. Failure of the single-pinned AFS samples: the plates slide out of the compression axis.

The experimental results for the single-pinned sample in comparison with the reference AFS are shown in Fig. C. 2. The results show that that the elastic modulus of the single-pinned AFS is higher than the reference sample one. However, the plateau stress of the single-pinned AFS is 52% reduced. At the strain values beyond 15%, the embedded pin into the AFS experiences an intensive buckling. The efficiency of the single-pinned AFS sample declines substantially due to the pin failure. Since the advantage of cellular materials is undergoing high levels of strain, practically using a single pin for Z-pinning the AFS is not efficacious. Multiple experiments of single-pinned AFS samples indicated the significant deficiency this Z-pinning layout.

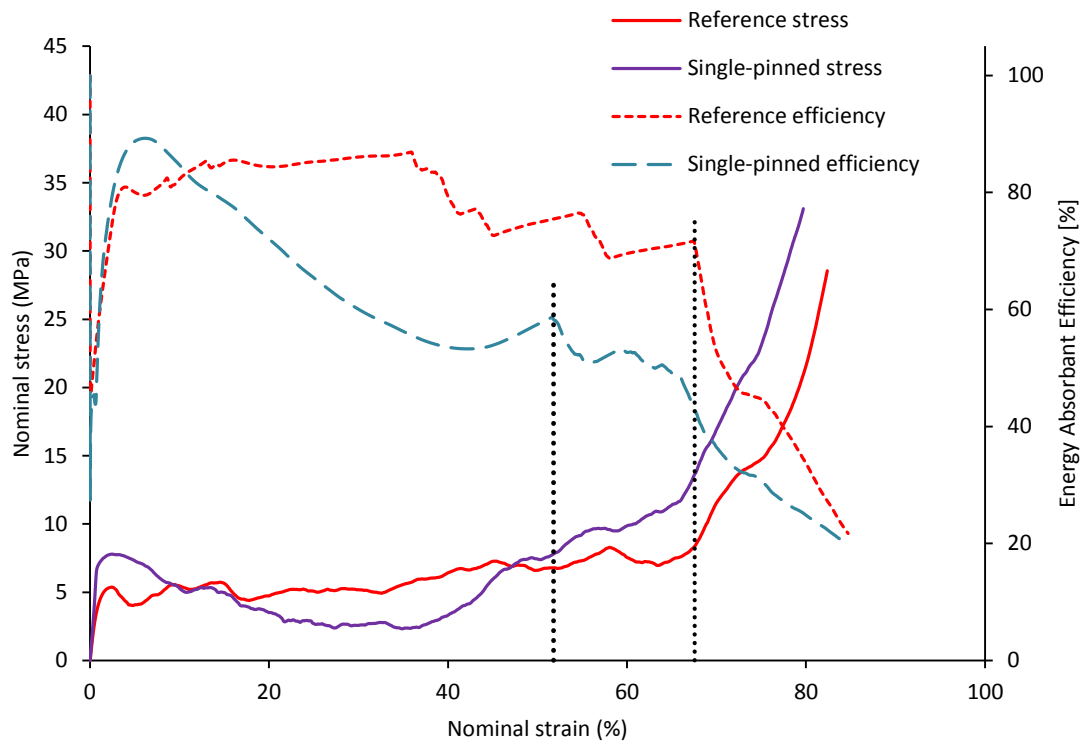


Fig. C. 2. Relationship between the energy absorption efficiency and the compressive stress for the reference AFS and the single-pinned AFS sample.

References

1. Gibson, L.J. and M.F. Ashby, *Cellular Solids: Structure and Properties*, second edition. 1997, Cambridge: Cambridge university press.
2. Hanssen, A.G., M. Langseth, and O.S. Hopperstad, *Static and dynamic crushing of circular aluminium extrusions with aluminium foam filler*. International Journal of Impact Engineering, 2000. **24**(5): p. 475-507.
3. Banhart, J., *Manufacture, characterisation and application of cellular metals and metal foams*. Progress in Materials Science, 2001. **46**(6): p. 559-632.
4. Kadkhodapour, J. and S. Raeisi, *Micro-macro investigation of deformation and failure in closed-cell aluminum foams*. Computational Materials Science, 2014. **83**: p. 137-148.
5. Fiedler, T., et al., *Dynamic compressive loading of expanded perlite/aluminum syntactic foam*. Materials Science and Engineering: A, 2015. **626**: p. 296-304.
6. Duarte, I., et al., *Failure Modes and Influence of the Quasi-static Deformation Rate on the Mechanical Behavior of Sandwich Panels with Aluminum Foam Cores*. Mechanics of Advanced Materials and Structures, 2010. **17**(5): p. 335-342.
7. Liu, Z., Z. Huang, and Q. Qin, *Experimental and theoretical investigations on lateral crushing of aluminum foam-filled circular tubes*. Composite Structures, 2017. **175**: p. 19-27.
8. Motz, C. and R. Pippan, *Deformation behaviour of closed-cell aluminium foams in tension*. Acta Materialia, 2001. **49**(13): p. 2463-2470.
9. Peroni, L., M. Avalle, and M. Peroni, *The mechanical behaviour of aluminium foam structures in different loading conditions*. International Journal of Impact Engineering, 2008. **35**(7): p. 644-658.
10. Taherishargh, M., et al., *Low-density expanded perlite-aluminium syntactic foam*. Materials Science and Engineering: A, 2014. **604**: p. 127-134.
11. Meguid, S.A., S.S. Cheon, and N. El-Abbasi, *FE modelling of deformation localization in metallic foams*. Finite Elements in Analysis and Design, 2002. **38**(7): p. 631-643.
12. Nammi, S.K., P. Myler, and G. Edwards, *Finite element analysis of closed-cell aluminium foam under quasi-static loading*. Materials & Design, 2010. **31**(2): p. 712-722.
13. Taherishargh, M., et al., *On the particle size effect in expanded perlite aluminium syntactic foam*. Materials & Design (1980-2015), 2015. **66**: p. 294-303.
14. Wan, L., et al., *Interfacial behavior and mechanical properties of aluminum foam joint fabricated by surface self-abrasion fluxless soldering*. Journal of Alloys and Compounds, 2016. **671**: p. 346-353.
15. Mu, Y., et al., *Deformation mechanisms of closed-cell aluminum foam in compression*. Scripta Materialia, 2010. **63**(6): p. 629-632.
16. Daoud, A., *Compressive response and energy absorption of foamed A359-Al₂O₃ particle composites*. Journal of Alloys and Compounds, 2009. **486**(1-2): p. 597-605.
17. Esmaeaelzadeh, S. and A. Simchi, *Foamability and compressive properties of AlSi7-3 vol.% SiC-0.5 wt.% TiH₂ powder compact*. Materials Letters, 2008. **62**(10-11): p. 1561-1564.
18. Lin, Y., Q. Zhang, and G. Wu, *Interfacial microstructure and compressive properties of Al-Mg syntactic foam reinforced with glass cenospheres*. Journal of Alloys and Compounds, 2016. **655**: p. 301-308.
19. Wang, J., et al., *A novel approach to obtain in-situ growth carbon nanotube reinforced aluminum foams with enhanced properties*. Materials Letters, 2015. **161**: p. 763-766.
20. Duarte, I., et al., *A novel approach to prepare aluminium-alloy foams reinforced by carbon-nanotubes*. Materials Letters, 2015. **160**: p. 162-166.
21. Luo, Y., et al., *Compressive property and energy absorption characteristic of open-cell SiCp/AlSi9Mg composite foams*. Journal of Alloys and Compounds, 2010. **499**(2): p. 227-230.

22. Liu, C., Y.X. Zhang, and J. Li, *Impact responses of sandwich panels with fiber metal laminate skins and aluminium foam core*. Composite Structures, 2017. **182**: p. 183-190.
23. An, Y., et al., *Investigating the internal structure and mechanical properties of graphene nanoflakes enhanced aluminum foam*. Materials & Design, 2017. **134**: p. 44-53.
24. Wang, N., et al., *Compressive performance and deformation mechanism of the dynamic gas injection aluminum foams*. Materials Characterization, 2019. **147**: p. 11-20.
25. Rathbun, H.J., et al., *Performance of metallic honeycomb-core sandwich beams under shock loading*. International Journal of Solids and Structures, 2006. **43**(6): p. 1746-1763.
26. Xue, Z. and J.W. Hutchinson, *Crush dynamics of square honeycomb sandwich cores*. International Journal for Numerical Methods in Engineering, 2006. **65**(13): p. 2221-2245.
27. Dharmasena, K.P., et al., *Dynamic compression of metallic sandwich structures during planar impulsive loading in water*. European Journal of Mechanics - A/Solids, 2010. **29**(1): p. 56-67.
28. Ajdari, A., H. Nayeab-Hashemi, and A. Vaziri, *Dynamic crushing and energy absorption of regular, irregular and functionally graded cellular structures*. International Journal of Solids and Structures, 2011. **48**(3): p. 506-516.
29. Guo, K., et al., *Experimental investigation on the dynamic behaviour of aluminum foam sandwich plate under repeated impacts*. Composite Structures, 2018. **200**: p. 298-305.
30. Zheng, Z., et al., *Dynamic stress-strain states for metal foams using a 3D cellular model*. Journal of the Mechanics and Physics of Solids, 2014. **72**: p. 93-114.
31. Deshpande, V. and N. Fleck, *High strain rate compressive behaviour of aluminium alloy foams*. International Journal of Impact Engineering, 2000. **24**(3): p. 277-298.
32. Liu, Y., et al., *A numerical study on the rate sensitivity of cellular metals*. International journal of solids and structures, 2009. **46**(22-23): p. 3988-3998.
33. Elnasri, I., et al., *Shock enhancement of cellular structures under impact loading: Part I Experiments*. Journal of the Mechanics and Physics of Solids, 2007. **55**(12): p. 2652-2671.
34. Mukai, T., et al., *Experimental study of energy absorption in a close-celled aluminum foam under dynamic loading*. Scripta Materialia, 1999. **40**(8).
35. Ruan, D., et al., *Compressive behaviour of aluminium foams at low and medium strain rates*. Composite Structures, 2002. **57**(1): p. 331-336.
36. Yaseer Omar, M., et al., *Syntactic foam core metal matrix sandwich composite: Compressive properties and strain rate effects*. Materials Science and Engineering: A, 2015. **643**: p. 156-168.
37. Jing, L., et al., *Compressive strain rate dependence and constitutive modeling of closed-cell aluminum foams with various relative densities*. Journal of Materials Science, 2018. **53**(20): p. 14739-14757.
38. Wang, B., et al., *Experimental investigation of 3D sandwich structure with core reinforced by composite columns*. Materials & Design, 2010. **31**(1): p. 158-165.
39. Liu, T., Z.C. Deng, and T.J. Lu, *Analytical modeling and finite element simulation of the plastic collapse of sandwich beams with pin-reinforced foam cores*. International Journal of Solids and Structures, 2008. **45**(18-19): p. 5127-5151.
40. Yalkin, H.E., B.M. Icten, and T. Alpyildiz, *Enhanced mechanical performance of foam core sandwich composites with through the thickness reinforced core*. Composites Part B: Engineering, 2015. **79**: p. 383-391.
41. Mouritz, A.P., *Compression properties of z-pinned sandwich composites*. Journal of Materials Science, 2006. **41**(17): p. 5771-5774.
42. Zhou, J., et al., *The energy-absorbing behaviour of foam cores reinforced with composite rods*. Composite Structures, 2014. **116**: p. 346-356.
43. Hibbit, H., B. Karlsson, and E. Sorensen, *ABAQUS user manual, version 6.12*. Simulia, Providence, RI, 2012.

44. Combaz, E., A. Rossoll, and A. Mortensen, *Hole and notch sensitivity of aluminium replicated foam*. Acta Materialia, 2011. **59**(2): p. 572-581.
45. Olurin, O.B., N.A. Fleck, and M.F. Ashby, *Deformation and fracture of aluminium foams*. Materials Science and Engineering: A, 2000. **291**(1-2): p. 136-146.
46. Xu, A., et al., *Finite element analysis of indentation of aluminium foam and sandwich panels with aluminium foam core*. Materials Science and Engineering: A, 2014. **599**: p. 125-133.
47. Rizov, V., A. Shipsha, and D. Zenkert, *Indentation study of foam core sandwich composite panels*. Composite Structures, 2005. **69**(1): p. 95-102.
48. Cho, J.U., et al., *Impact fracture behavior at the material of aluminum foam*. Materials Science and Engineering: A, 2012. **539**: p. 250-258.
49. Zhu, X., et al., *Collapse models of aluminum foam sandwiches under static three-point bending based on 3D geometrical reconstruction*. Computational Materials Science, 2014. **85**: p. 38-45.
50. Bastawros, A.F., H. Bart-Smith, and A.G. Evans, *Experimental analysis of deformation mechanisms in a closed-cell aluminum alloy foam*. Journal of the Mechanics and Physics of Solids, 2000. **48**(2): p. 301-322.
51. McCullough, K.Y.G., N.A. Fleck, and M.F. Ashby, *Toughness of aluminium alloy foams*. Acta Materialia, 1999. **47**(8): p. 2331-2343.
52. Raeisi, S., *Investigation on mechanical properties of bio-inspired porous materials using numerical methods and experimental data*, in *Mechanical Engineering*. 2014, Shahid Rajee Teacher Training University: Tehran. p. 130.
53. Bart-Smith, H., et al., *Compressive deformation and yielding mechanisms in cellular Al alloys determined using X-ray tomography and surface strain mapping*. Acta Materialia, 1998. **46**(10): p. 3583-3592.
54. Palazotto, A.N., et al., *Low velocity impact damage characteristics of Z-fiber reinforced sandwich panels — an experimental study*. Composite Structures, 1998. **43**(4): p. 275-288.
55. Ashby, M.F., et al., *Metal foams: a design guide*. 2000: Elsevier.
56. Baumeister, J., J. Banhart, and M. Weber, *Aluminium foams for transport industry*. Materials & Design, 1997. **18**(4-6): p. 217-220.
57. Li, Q.M., I. Magkiriadis, and J.J. Harrigan, *Compressive Strain at the Onset of Densification of Cellular Solids*. 2006. **42**(5): p. 371-392.
58. R. Florek, F.S., M. Nosko, J. Harnúšková, *Compression test evaluation method for aluminium foam parts of different alloys and densities*. Powder Metallurgy Progress, 2010. **10**: p. 207-212.